Perfusion characteristics of the human hepatic microcirculation based on 3D reconstructions and computational fluid dynamic analysis

---

Charlotte Debbaut[1], Jan Vierendeels[2], Christophe Casteleyn[3], Pieter Cornillie[4], Denis Van Loo[5,6], Paul Simoens[4], Luc Van Hoorebeke[5], Diethard Monbaliu[7] and Patrick Segers[1]

[1] Biofluid, Tissue and Solid Mechanics for Medical Applications (bioMMeda), Institute Biomedical Technology, Ghent University. De Pintelaan 185 – Block B, B-9000 Gent, Belgium
Email: charlotte.debbaut@ugent.be; telephone: (0032) 9 332 33 79

[2] Department of Flow, Heat and Combustion Mechanics, Ghent University. Sint-Pietersnieuwstraat 41, B-9000, Gent, Belgium

[3] Laboratory for Veterinary Anatomy, Embryology & Pathology, Department of Veterinary Sciences, Faculty of Pharmaceutical, Biomedical and Veterinary Sciences, University of Antwerp. Universiteitsplein 1, 2610 Wilrijk, Belgium

[4] Department of Morphology, Faculty of Veterinary Medicine, Ghent University. Salisburylaan 133, B-9820 Merelbeke, Belgium

[5] Centre for X-Ray Tomography, Department of Physics and Astronomy, Ghent University. Proeftuinstraat 86, B-9000 Gent, Belgium

[6] Department of Soil Management, Ghent University. Coupure links 653, B-9000 Gent, Belgium

[7] Department of Abdominal Transplant Surgery, University Hospitals Leuven, Catholic University Leuven. Herestraat 49, B-3000 Leuven, Belgium

Abstract

Background. The perfusion of the liver microcirculation is often analyzed in terms of idealized functional units (hexagonal liver lobules) based on a porous medium approach. More elaborate research is essential to assess the validity of this approach and to provide a more adequate and quantitative characterization of the liver microcirculation. To this end, we modeled the perfusion of the liver microcirculation using an image-based 3D reconstruction of human liver sinusoids and computational fluid dynamics techniques.

Method of Approach. After vascular corrosion casting, a microvascular sample (± 0.134 mm^3) representing 3 liver lobules, was dissected from a human liver vascular replica and scanned using a high resolution (2.6 µm) micro-CT scanner. Following image processing, a cube (0.15x0.15x0.15 mm^3) representing a sample of intertwined and interconnected sinusoids, was isolated from the 3D reconstructed dataset to define the fluid domain. Three models were studied to simulate flow along 3 orthogonal directions (i.e. parallel to the central vein and in the radial and circumferential directions of the lobule). Inflow and outflow guidances were added to facilitate solution convergence, and good quality volume meshes were obtained using approximately 9 million tetrahedral cells. Subsequently, 3 computational fluid dynamics models were generated and solved assuming Newtonian liquid properties (viscosity 3.5 mPa·s). Post-processing allowed to visualize and quantify the microvascular flow characteristics, to calculate the permeability tensor and corresponding principal permeability axes as well as the 3D porosity.

Results. The computational fluid dynamics simulations provided data on pressure differences, preferential flow pathways and wall shear stresses. Notably, the pressure difference resulting from the flow simulation parallel to the central vein (0 - 100 Pa) was clearly smaller than the difference from the radial (0 – 170 Pa) and circumferential (0 – 180 Pa) flow directions. This resulted in a higher permeability along the central vein direction ($k_{d,33} = 3.64 \cdot 10^{-14}$ m²) in comparison with the radial ($k_{d,11} = 1.56 \cdot 10^{-14}$ m²) and circumferential ($k_{d,22} = 1.75 \cdot 10^{-14}$ m²) permeabilities which were approximately equal. The mean 3D porosity was 14.3%.

Conclusions. Our data indicate that the human hepatic microcirculation is characterized by a higher permeability along the central vein direction, and an about two times lower permeability along the radial and circumferential directions of a lobule. Since the permeability coefficients depend on the flow direction, (porous medium) liver microcirculation models should take into account sinusoidal anisotropy.

Keywords. Human liver microcirculation, computational fluid dynamics, wall shear stress, permeability tensor, porosity

1. Introduction

The blood flow through the liver is known to be unique and complex, especially at the level of the microcirculation due to the fact that the liver receives blood from the hepatic artery (HA) and the portal vein (PV) [1-6]. The HA and PV vascular trees branch until they reach the microcirculation at the level of the so-called hepatic functional units, typically considered as hexagonal lobules [7-9]. In this conceptual model, each lobule receives blood from its periphery through the hepatic arterioles and portal venules located in each of the portal triads (Fig. 1). At the level of the lobules, HA and PV blood is mixed in the sinusoids (hepatic-specific capillaries) where the metabolic activity and exchange of nutrients, oxygen etc. with the hepatocytes takes place. Subsequently, the blood is drained radially towards the central veins. These veins cluster until they reach the outflow hepatic veins (HV) and the vena cava inferior [1, 9].

Despite the fact that this conceptual model of liver functional units is widely used, liver perfusion is still relatively poorly understood. This has implications for several liver-related research areas. In liver transplantation research, the optimal conditions to preserve and perfuse donor livers, when livers are subjected to (hypothermic) machine perfusion, are still poorly defined [10-17]. Moreover, the hemodynamic influence of complications such as portal hypertension and the small-for-size syndrome induced by living donor liver transplantation is being investigated [18-20]. In addition, similar questions arise in the case of liver pathologies (cirrhosis, steatosis etc.) influencing the liver perfusion, ablation treatments for hepatocellular tumors, diagnosis etc. [21, 22].

Numerical models may be an important tool to study liver perfusion on different scales (macrocirculation versus microcirculation), and lead to a better understanding of the organ's hemodynamics. Existing liver circulation models, however, mainly focus on the liver macrovasculature, representing the branching of the HA, PV and HV vessels [23-27]. In contrast, only a few studies have been performed on the liver microcirculation, i.e. the sinusoids between the portal tracts and the central veins within the lobules (Fig. 1). These studies were usually based on idealized geometries and the conceptual hexagonal liver lobule model. Rani et al. [28] studied the hepatic microcirculation using finite volume blood flow simulations in an idealized 3D segment of a hepatic lobule including a terminal HA, PV, HV and fenestrated sinusoidal space. Ricken et al. [29] developed an idealized 2D model of the blood flow through a longitudinal transection of liver lobules using a transverse isotropic permeability in the direction of the central vein. Furthermore, a 2D porous model of the blood flow through a hexagonal lobule transection was developed by Bonfiglio et al. [30], assuming an isotropic permeability and porosity for their first model, and an anisotropic permeability (radial versus circumferential) but isotropic porosity for a second model. Wambaugh et al. [31] and Shah et al. [32] used a graphical model with a discrete topology of the sinusoidal network to simulate the portal to centrilobular mass transfer of chemicals in a virtual tissue representing a hepatic lobule.

The sinusoidal microvasculature is thus often modeled as a porous medium with an isotropic permeability and/or porosity, an assumption which, to our knowledge, has never been validated. In addition, (human) liver microvascular flow has so far only been studied based on idealized geometries.

The aim of the present study is to numerically model the blood flow in the human hepatic sinusoidal microcirculation based on micro-CT images of real 3D sinusoidal geometries of a human liver, using computational fluid dynamic methods. Moreover, we investigated whether modeling the hepatic sinusoidal microvasculature as a homogeneous isotropic material is a valid approach by calculating the sinusoidal porosity as well as the permeability tensor of the tissue.

2. Materials and methods

This study was executed using a human liver discarded for transplantation after failed rescue allocation by Eurotransplant (Leiden, The Netherlands). As part of research related to machine perfusion preservation of the liver, this study was approved by the Ethical Committee of the University Hospitals Leuven (Belgium) and by the Belgian Liver and Intestine Committee. To obtain the numerical microcirculation model and the corresponding results, several steps were taken as described below: (1) vascular corrosion casting and micro-CT imaging to acquire the sinusoidal geometry; (2) image processing to calculate the 3D morphology; (3) the generation of the meshes for the computational fluid dynamics calculations; (4) defining the boundary conditions for the simulations and post-processing of the data; (5) calculation of the permeability tensor.

2.1 Vascular corrosion casting and micro-CT imaging

The human liver used for this study was recuperated from a human donor discarded for transplantation based on strict medical criteria (in this case because of steatosis). Although discarded, the liver showed no evidence of relevant anatomical or vascular differences compared to healthy livers. After resection of the liver from the donor body, the liver was preserved using hypothermic machine perfusion (HMP) as described in [24]. Even though the advantage of HMP is that the microvasculature is kept open and intact, the combination of HMP and casting might have had an effect on the microcirculation. Nevertheless, the dimensions of the sinusoids were in good agreement with the sinusoidal dimensions found in literature [1, 6, 33].

The goal of the vascular corrosion casting procedure was to obtain a replica of the vascular trees of a human liver. A human liver with a normal macroscopic appearance was simultaneously injected with a polymer through the HA and the PV. The injection fluid contained Batson's #17 monomer solution (100 parts), Batson's catalyst (15 parts), Batson's promoter (1 part) (Polysciences, Warrington, USA) and monomeric methyl methacrylate (20 parts) (Merck, Darmstadt, Germany). The liver was injected until sufficient quantities of resin were emerging from the HV. Subsequently, all vessels were clamped and the injected fluid polymerized during a period of approximately 2 hours. Afterwards, the liver tissue was macerated in potassium hydroxide (25% KOH) to generate the polymerized vascular replica. More elaborate details about the vascular corrosion casting procedure can be found in [24].

A small volume sample (± 0.134 mm^3), obtained from the left liver lobe was dissected from the liver cast and imaged using a scanning electron microscope (SEM; JEOL JSM 5600 LV, Jeol, Zaventem, Belgium) to verify whether the liver sinusoids were sufficiently casted. This resulted in the SEM image of the geometry shown in Fig. 2a. The intertwined and interconnected liver sinusoids are clearly visible, giving evidence of a liver cast of which the microcirculation was clearly filled with the injected polymer. The sample was subsequently scanned with an in-house developed high-resolution micro-CT scanner to obtain the 3D geometry with a resolution of 2.6 µm (see [24] for more information).

2.2 Image processing

The digital micro-CT datasets were processed using the software package Mimics (Materialise, Leuven, Belgium). The dataset was segmented based on its grey values to extract the features of the liver lobules and sinusoids, and a 3D reconstruction was calculated, leading to the visualization of three liver lobules (see Fig. 2a) or three primary modules according to Teutsch [7]. Because of the total dataset size and computer performance restrictions as well as computational costs, a sample was “virtually” dissected (Fig. 2b and 3) by calculating the intersection between a cube with predefined dimensions (0.15 x 0.15 x 0.15 mm^3) and a lobule by using Magics (Materialise, Leuven, Belgium). As such, the fluid domain for the computational fluid dynamics model was created. However, it was not straightforward to identify the individual classical liver lobules in the dataset (hexagonal prism-like structures; Fig. 1 and 3), since it was difficult to localize the portal triads (consisting of the terminal branches of the HA and PV as well as the intrahepatic bile ductules) at the boundaries of the lobules in a human liver (lobules are clearer delineated by connective tissue in other species such as rat and porcine livers). The final segmentation was based on the identification of the vascular septa in between lobules which appeared brighter on the micro-CT images. This was due to contrast agent particles added to the HA casting injectate. These particles were probably captured before entering the sinusoids because of their particle size and, hence, delineated the lobule boundaries. As illustrated in Fig. 3, the dissected cube was oriented such that the origin (0,0,0) was at the center of the sample and its z axis was approximately parallel to the direction of the central vein (i.e. longitudinally according to the liver lobule schematic with a hexagonal prism-like geometry). In addition, its transections perpendicular to the z axis were located in the area which we considered to be in between the central vein and the HA and PV at the portal triads. This resulted in the r and θ axis being oriented along the radial and circumferential directions, respectively, according to the hexagonal transection of the lobule (Fig. 3).

2.3 Mesh generation

As we wish to assess the complete permeability tensor of the sample (see also 2.5), three computational fluid dynamics cases (and meshes) were developed corresponding to a simulation of flow in the r, θ and z directions, respectively. For each of the setups, a dedicated simulation geometry needed to be created. An inflow and outflow box was added (height being 10% of the sample height) as a flow guidance proximal to the inlet and distal to the outlet, respectively (Fig. 2b). This was done to avoid convergence problems caused by too many inlets and outlets, as well as to avoid forcing a predefined flow through the inlet sinusoids [34].

The obtained surface geometries were processed using 3-Matic (Materialise, Leuven, Belgium) to provide good quality surface meshes of the fluid domain. First, “noise shells” were removed (e.g. a part of a bisected sinusoid which is not attached to the rest of the sinusoidal fluid domain). Subsequently, the meshes were improved by removing double or intersecting triangles and filling small holes which may originate from mesh manipulations. Next, the geometries were remeshed with a maximum triangle edge length of 1.2 µm to capture the morphological features of the geometries studied, followed by a quality preserving reduction of triangles. To this purpose, some channels with a very small diameter had to be refined because they would otherwise collapse during the remeshing procedure. In a last step, the surface meshes were further manually improved to result in a surface mesh of which all triangles had a skewness less than 0.6. The resulting surface meshes were then exported to TGrid (Ansys, Canonsburg, PA, USA) to generate volume meshes. The volume meshes consisted of tetrahedral cells with a maximal skewness less than 0.95. The resulting meshes existed of approximately 1 million triangular surface elements and 9 million tetrahedral volume elements clearly capturing the sinusoidal geometrical features (Fig. 2b).

2.4 Computational fluid dynamics simulations & post-processing

The steady and laminar computational fluid dynamics models were solved using Fluent (Ansys, Canonsburg, PA, USA). The inlet boundary condition consisted of a flat velocity profile at the top plane of the inflow guidance (plane defined by a r, θ, z coordinate equal to 90 µm for the r, θ, z flow simulation, respectively; see Fig. 2). Since there are, to the authors' knowledge, no literature data available on the flow velocities in three orthogonal directions for the human hepatic microcirculation, the applied velocity was estimated by scaling down the total liver blood flow to the flow through the sample studied (eq. 1). This was done by using literature values of the average human liver blood flow Q_{liver} (1450 ml/min), the average liver mass m_{liver} (1.4 kg) [9], density ρ (1000 kg/m³ equal to water) and the dimensions of the sample studied (volume $V_{sample} = 0.15^3$ mm³; area of inflow plane $A_{sample} = 0.15^2$ mm²). Using eq. 2, this resulted in a velocity inlet v of $2.59 \cdot 10^{-6}$ m/s.

$$Q_{sample} = Q_{liver} \frac{\rho \cdot V_{sample}}{m_{liver}} \tag{1}$$

$$v = \frac{Q_{sample}}{A_{sample}} \tag{2}$$

As outlet boundary condition, a pressure outlet of 0 Pa was used at the bottom (plane defined by a r, θ, z coordinate equal to -90 µm for the r, θ, z flow simulation, respectively; Fig. 2b). The lateral boundaries existing of transected sinusoids were set to symmetry boundary conditions implying no flux perpendicular to these planes. The sinusoidal lumen was modeled as a closed wall (no slip). Blood was modeled as an incompressible Newtonian fluid with a density of 1050 kg/m³ and a dynamic viscosity µ of $3.5 \cdot 10^{-3}$ Pa·s [23].

Tecplot (Tecplot Inc., Bellevue, WA) was used to process, calculate and visualize the hemodynamic parameters of interest such as pressure difference, flow velocity, wall shear stress, flow trajectories, etc.

2.5 Calculation of the permeability tensor

Subsequently, the permeability tensor K (eq. 3; [35]) was assessed to quantify the permeable behavior of the sinusoidal perfusion in different directions for the dissected sample (Fig. 3). The permeability tensor defines the permeability of the tissue in the r, θ or z direction caused by the pressure difference in the r, θ or z direction. For instance, $k_{r\theta}$ specifies the permeability along the r direction due to the pressure difference in the θ direction [35].

$$K = \begin{bmatrix} k_{rr} & k_{r\theta} & k_{rz} \\ k_{\theta r} & k_{\theta\theta} & k_{\theta z} \\ k_{zr} & k_{z\theta} & k_{zz} \end{bmatrix} \tag{3}$$

The permeability tensor is calculated based on Darcy's law, which describes the fluid flow through a porous medium (eq. 4 with P the pressure [Pa], µ the dynamic viscosity [Pa·s], k the permeability [m²] and v the velocity [m/s]).

$$\nabla P = -\frac{\mu}{k}\vec{v} \tag{4}$$

Darcy's law can be rewritten for every pressure difference direction separately inducing fluid flow in the r, θ and z direction. This is illustrated in eq. 5-7 for a pressure difference in the r direction with L [m] the characteristic length of the sample studied.

$$\frac{\Delta P_r}{L_r} = -\frac{\mu}{k_{rr}}\vec{v}_r \tag{5}$$

$$\frac{\Delta P_r}{L_r} = -\frac{\mu}{k_{\theta r}}\vec{v}_\theta \tag{6}$$

$$\frac{\Delta P_r}{L_r} = -\frac{\mu}{k_{zr}}\vec{v}_z \tag{7}$$

The velocity magnitude in eq. (5-7) can be calculated as the corresponding flow Q [m³/s] divided by the area A [m²]. This is illustrated in eq. (8-10) in which Darcy's law is rearranged to calculate the corresponding permeability coefficients for the pressure difference in the r direction.

$$k_{rr} = -\mu \frac{L_r}{\Delta P_r}\frac{Q_r}{A_r} \tag{8}$$

$$k_{\theta r} = -\mu \frac{L_r}{\Delta P_r}\frac{Q_\theta}{A_\theta} \tag{9}$$

$$k_{zr} = -\mu \frac{L_r}{\Delta P_r}\frac{Q_z}{A_z} \tag{10}$$

For each of the 3 computational fluid dynamics cases (simulation of flow in the r, θ and z direction), fifteen cubic samples with a characteristic length of 50 µm were studied to determine the permeability tensor to allow for some statistical sampling of the simulated specimen. The cubes were defined by the coordinates as shown in Table 1. They were positioned such that they did not include the boundary regions, since the flow behavior in those regions is influenced by the prescribed lateral boundary conditions (symmetry; no flux). For every cubic sample, all permeability coefficients were calculated based on eq. (8-10). The pressure differences ΔP were calculated by subtracting the mean pressure of the inflow plane of the studied cubic sample from the mean pressure of the outflow plane (eq. 11 for the r direction).

$$\Delta P_{\mathrm{r}} = P_{\mathrm{r,inflow}} - P_{\mathrm{r,outflow}} \tag{11}$$

The characteristic lengths L (50 µm) and areas A ($2.5\cdot10^{-3}$ mm²) were equal for all cubes since they had the same dimensions. The flow Q in eq. 8-10 was calculated as the average flow of the volumetric flows through 5 parallel planes equally distributed over the length of the cube and perpendicular to the permeability direction studied. This was implemented in Fluent by writing journal files to obtain the necessary bounded planes.

After calculating the permeability tensor for every separate cube, the mean, standard deviation and median values of all permeability coefficients were determined. The normality of the distribution of the permeability coefficients was verified by means of a Shapiro-Wilk test using SPSS (IBM, Armonk, New York, United States).

Additionally, the principal axes (defined by the eigenvectors) as well as the permeability values in the principal directions were calculated from the permeability tensor K (see Appendix for the linear algebraic equations). This allows to quantify the angles between the original coordinate system axes and the principal axes of the permeability tensor.

Finally, the 3D sinusoidal porosity was also determined (using Magics software) for every cube (as defined by the coordinates in Table 1) by dividing the volume occupied by the sinusoids by the volume of the cube studied (eq. 12).

$$\varepsilon = \frac{V_{\mathrm{sinusoids}}}{V_{\mathrm{cube}}} \tag{12}$$

Results

3.1 Computational fluid dynamics simulations: hemodynamic analysis

The computational fluid dynamics simulation results are represented in Figs. 4-7. Figure 4 illustrates the static pressure visualization on the boundaries of the 3 cases. The pressure differences over the cube along the r and θ flow directions are very similar (approximately ranging from 0 to 170 Pa and 0 to 180 Pa, respectively). In contrast, the pressure difference for the simulation of blood flow in the z-direction is clearly smaller (0-100 Pa), while applying the same boundary conditions as in the r and θ flow simulations (velocity inlet of $2.59 \cdot 10^{-6}$ m/s at the top and zero pressure outlet at the bottom).

As visualized in Fig. 4, the pressure drops significantly through certain sinusoids and stays almost constant throughout others. This corresponds to the typical presence of preferential pathways in the sinusoidal geometry along tracks with relevant pressure drops. Figure 5 depicts some of these preferential streamlines colored by their velocity magnitude. The preferential paths seem to be mainly concentrated in the middle region of the geometry, and not at locations near to the transected sinusoids delineating the lateral boundaries. This is obviously a consequence of the symmetry boundary condition applied at the sides. The velocity magnitude approximately ranges from 0 to $1.4 \cdot 10^{-3}$ m/s, 0 to $2.6 \cdot 10^{-3}$ m/s, 0 to $1.1 \cdot 10^{-3}$ m/s for the case of a pressure difference in the r, θ, z directions, respectively. The mean velocity in all of these cases is typically at the lower end of these ranges as can be deducted from the streamlines in Fig. 5.

Since the boundary conditions are likely to influence the solution, data of a smaller central cube of 50 µm (cube 1 as defined in Table 1) are further analyzed to minimize the boundary induced effects. The velocity magnitude in the smaller cube has a mean value of $1.0 \cdot 10^{-4}$ m/s, $7.3 \cdot 10^{-5}$ m/s, $7.7 \cdot 10^{-5}$ m/s for the r, θ, z flow simulations, respectively.

For the major part of the model boundaries, wall shear stress remains below 1 Pa for each of the simulations (Fig. 6). At narrow channel locations, however, higher values are found. Histograms of the wall shear stress distribution for the central cube (cube 1 in Table 1) are depicted in Fig. 7. Overall, very low wall shear stresses cover the major part of the sinusoidal lumen surface. The mean wall shear stress in the central cube for the r, θ and z simulation was 0.42 Pa, 0.31 Pa, and 0.28 Pa, respectively. The corresponding local maximum wall shear stress was 6.62 Pa, 4.19 Pa, and 3.80 Pa, respectively.

3.2 Porosity and permeability tensor

The sinusoidal porosity was calculated for every cube as defined by the coordinates in Table 1, and values are depicted in the last column of Table 2. The resulting mean porosity was 14.3% ± 2.8%.

The components of the permeability tensor for each of the 15 subsampled cubes are given in Table 2. As the Shapiro-Wilk test indicated that the distribution of the resulting permeability coefficients was not normal for 4 out of 9 coefficients (significance level of 0.1; see Table 2), the overall permeability tensor for the sample is best based on the median values (as shown in eq. 13) to avoid a large influence of outlier values.

$$K=\begin{bmatrix} k_{rr} & k_{r\theta} & k_{rz} \\ k_{\theta r} & k_{\theta\theta} & k_{\theta z} \\ k_{zr} & k_{z\theta} & k_{zz} \end{bmatrix}=\begin{bmatrix} 1.78\cdot 10^{-14} & -1.29\cdot 10^{-15} & -7.20\cdot 10^{-15} \\ 1.07\cdot 10^{-15} & 1.76\cdot 10^{-14} & -1.06\cdot 10^{-15} \\ -5.45\cdot 10^{-15} & 2.73\cdot 10^{-15} & 3.43\cdot 10^{-14} \end{bmatrix} \qquad (13)$$

Calculating the eigenvectors of the permeability tensor as illustrated in the Appendix, resulted in the principal axes determined by the eigenvectors ($\vec{e}_1, \vec{e}_2, \vec{e}_3$) in matrix V (eq. 14) and the corresponding diagonal matrix K$_d$ with the permeability values along the principal axes (eq. 15).

$$V=\begin{bmatrix}\vec{e}_1 & \vec{e}_2 & \vec{e}_3\end{bmatrix}=\begin{bmatrix} 0.943 & 0.0924 & -0.320 \\ -0.0827 & 0.996 & 0.0438 \\ 0.323 & -0.0148 & 0.946 \end{bmatrix} \qquad (14)$$

$$K_d=\begin{bmatrix} k_{d,11} & 0 & 0 \\ 0 & k_{d,22} & 0 \\ 0 & 0 & k_{d,33} \end{bmatrix}=\begin{bmatrix} 1.56\cdot 10^{-14} & 0 & 0 \\ 0 & 1.75\cdot 10^{-14} & 0 \\ 0 & 0 & 3.64\cdot 10^{-14} \end{bmatrix} \qquad (15)$$

Using these results, the angles between the original coordinate system axes and the principal axes were 19.5°, 5.4° and 18.9° for the r, θ and z axes, respectively. The principal axes coordinate system would thus be obtained by rotating the original orthogonal coordinate system approximately -19° around the θ axis. In addition, the permeability coefficients in the principal directions (diagonal coefficients of K$_d$) show that the permeability in the central vein direction ($k_{d,33} = 3.64\cdot 10^{-14}$ m²) is higher than the corresponding permeabilities in the radial and circumferential directions ($k_{d,11} = 1.56\cdot 10^{-14}$ m² and $k_{d,22} = 1.76\cdot 10^{-14}$ m², respectively) which are almost equal.

Discussion

In this paper, a numerical model of the human liver microcirculation has been developed based on a 3D image-based geometry of the liver sinusoids, and was used to study the fluid mechanical characteristics of perfusion at the sinusoidal level. The model presented in this study is, to the best of our knowledge, unique in its kind and provides a further step towards a more quantitative assessment of the perfusion properties of the liver microcirculation.

The sample that formed the basis of the model was obtained from a cast of the human liver, and oriented such that - bearing in mind the functional liver lobule unit - the z-axis was approximately aligned parallel to the central vein. Our data indicate that the pressure difference in the z direction is typically smaller than those in the r and θ directions. Since the pressure difference can be interpreted as a degree of resistance to flow (given the same boundary conditions in all 3 cases), the resistance to flow is smallest in the z direction. This corresponds with the resulting diagonal permeability tensor K_d in which $k_{d,33}$ is clearly larger than $k_{d,11}$ and $k_{d,22}$ (which are approximately equal), implying highest permeability of the liver lobule parallel to the direction of the central vein ($k_{d,33}$). Radial ($k_{d,11}$) and circumferential ($k_{d,22}$) permeabilities, as seen in the plane of a hexagonal transection of a lobule, are of a similar magnitude (Fig. 3). Since rotating the original coordinate system -19° around the θ axes approximately equals the principal axes determined by the eigenvectors, this suggests that the orientation and corresponding coordinate system as applied in this study, are reasonably well aligned along the principal directions of permeability. The immediate result of these findings is that the sinusoidal circulation is clearly anisotropic. Consequently, the assumption of a homogeneous isotropic tissue seems insufficient to describe the porous behavior of the sinusoidal microvasculature.

Given the fact that the study is based on one sample from one human liver cast, results should be interpreted as indicative and one should be reluctant to generalize our findings. More samples might allow a better estimation of these characteristics and identify potential regional heterogeneities in tissue properties of the liver under study, but imply a very labor-intensive procedure to acquire good geometries and meshes. Consequently, only one sample was studied, of which, however, subsamples were used to characterize the permeability of liver tissue. Care was taken to make sure that the sinusoidal heterogeneity was sufficiently covered when selecting the sample to study. A cube with dimensions of 0.15 x 0.15 x 0.15 mm^3 seemed to be sufficient to capture the heterogeneity of tortuous and interconnected sinusoids.

In the process of developing the computational fluid dynamics model geometry, it was inevitable to make compromises and take decisions that have an impact (which we tried to minimize) on the simulation results. Some sinusoids, for instance, were cut when dissecting the cubic sample. As a consequence, these transection planes of bisected sinusoids had to be defined as a boundary condition. Symmetry conditions were applied resulting in no flux through the boundary sections. However, in reality these sinusoids are continuous and flux is possible. To minimize the influence of these boundary induced effects on the results, we limited the quantitative analyses to cubes at a certain minimal distance (25 µm which is equal to 16.6% of the characteristic length of 0.15 mm) from these boundaries (Table 1).

In this study, blood is modeled as an incompressible and Newtonian fluid with a constant density and dynamic viscosity. It is, however, known that the hemodynamic behavior of blood at the microcirculation level is different from the behavior at the macrocirculation level (non-Newtonian fluid, Fahraeus-Lindqvist effect [36]). However, the assumption of an incompressible and Newtonian fluid is justified for this study, since we are interested in investigating the permeability tensor, which is independent of the fluid studied, because permeability is a purely geometrically determined parameter. The reported shear stress levels, on the other hand, might not fully reflect the hemodynamic stress exerted by the blood in-vivo. Note, however, that they might be indicative of shear stress exerted by blood-mimicking liquids upon machine perfusion of isolated organs for transplantation.

Our model and results can be compared with some studies based on idealized microcirculation models, in particular the 2D models of Ricken et al. [29] and Bonfiglio et al. [30]. However, both 2D models lack one dimension which has a non-negligible influence on the resulting flow behavior. The model of Ricken et al. [29] does take into account longitudinal sections of idealized lobules with the central veins and hepatic arterioles, while modeling the liver microcirculation using a biphasic approach. On the contrary, the model of Bonfiglio et al. [30] focuses on the hexagonal transection of a liver lobule to build a porous medium model of the liver microcirculation. In this study, a porosity estimate (ε = 12%) based on brain tissue imaging [37], was used to calculate the corresponding sinusoidal permeability. This value is somewhat lower than the porosity acquired in our study (14.3% ± 2.8%).

The results of our study can lead to new, improved models using porous media to simulate the behavior of the liver microcirculation taking into account the anisotropy. Moreover, these models could also be applied to liver perfusion settings other than the natural blood flow, such as the hemodynamic conditions experienced by the microcirculation in the case of liver pathologies, treatments and transplantation procedures such as machine perfusion preservation, ischemia reperfusion…

Conclusion

Vascular corrosion casting and micro-CT scanning allowed to construct a 3D numerical microcirculation model of a human liver. Our data indicate that the human hepatic microcirculation clearly displays anisotropic behavior in terms of permeability, which was quantified by means of a permeability tensor. In particular, a higher permeability was demonstrated along the direction of the central vein, and about two times lower but approximately equal permeabilities along the radial and circumferential directions of the liver lobule. Since the permeability coefficients depend on the flow direction, liver microcirculation models should take into account sinusoidal anisotropy.

Acknowledgments

This research was supported by the Agency for Innovation by Science and Technology in Flanders (IWT), Belgium. The authors would also like to thank Valeer Desmet, Frédéric Maes, Jennifer Siggers and Rodolfo Repetto for their contributions.

Nomenclature

2D = 2-dimensional

3D = 3-dimensional

A [m^2] = area

CT = computer tomography

HA = hepatic artery

HV = hepatic veins

K = permeability tensor

KOH = potassium hydroxide

L [m] = length

P [Pa] = pressure

PV = portal vein

Q [m^3/s] = flow

V [m^3] = volume

$\vec{e}_1$ = eigenvector

k [m^2] = permeability coefficient

m [kg] = mass

$\vec{v}$ = velocity vector

α [°] = angle

ε = porosity

λ = eigenvalue

μ [Pa·s] = dynamic viscosity

ρ [kg/m^3] = density

Appendix: calculation of the principal axes of the permeability tensor

To determine the principal axes and principal permeabilities of tensor K, the eigenvalues as well as the eigenvectors had to be calculated. As illustrated in Liakopoulos et al. [35], a permeability tensor has to be a symmetric matrix. Accordingly, a real symmetric matrix has real eigenvalues and real eigenvectors corresponding to an orthogonal coordinate system representing the principal axes [38]. As such, the symmetric part of K was defined by calculating the mean values of the off-diagonal coefficients as illustrated for $k_{r\theta}$ and $k_{\theta r}$ in eq. 16. This operation resulted in a symmetric matrix K_{symm} as defined in eq. 17.

$$k_{symm,r\theta} = \frac{k_{r\theta} + k_{\theta r}}{2} \tag{16}$$

$$K_{symm} = \begin{bmatrix} k_{rr} & k_{symm,r\theta} & k_{symm,rz} \\ k_{symm,r\theta} & k_{\theta\theta} & k_{symm,\theta z} \\ k_{symm,rz} & k_{symm,\theta z} & k_{zz} \end{bmatrix} \tag{17}$$

Subsequently, the eigenvalues (λ_1, λ_2, λ_3) were calculated by solving the characteristic polynomial of K_{symm} (eq. 18), and accordingly, the eigenvectors ($\vec{e}_1, \vec{e}_2, \vec{e}_3$) being the directions of the principal axes belonging to K_{symm}, were determined (eq. 19).

$$\det(K_{symm} - \lambda I) = \begin{vmatrix} k_{rr} - \lambda & k_{symm,r\theta} & k_{symm,rz} \\ k_{symm,r\theta} & k_{\theta\theta} - \lambda & k_{symm,\theta z} \\ k_{symm,rz} & k_{symm,\theta z} & k_{zz} - \lambda \end{vmatrix} = 0 \tag{18}$$

$$(K_{symm} - \lambda I) \cdot \vec{e} = 0 \tag{19}$$

Using the eigenvectors (columns of matrix V; eq. 20), K_{symm} was diagonalized resulting in the diagonal matrix K_d (eq. 20). This matrix represents the principal permeabilities belonging to the principal axes defined by the eigenvectors.

$$K_d = V^T K_{symm} V = \begin{bmatrix} \vec{e}_1 \\ \vec{e}_2 \\ \vec{e}_3 \end{bmatrix} K_{symm} \begin{bmatrix} \vec{e}_1 & \vec{e}_2 & \vec{e}_3 \end{bmatrix} = \begin{bmatrix} k_{d,11} & 0 & 0 \\ 0 & k_{d,22} & 0 \\ 0 & 0 & k_{d,33} \end{bmatrix} \tag{20}$$

Knowing the eigenvectors and accompanying diagonal matrix, we were able to calculate the angles between the predefined coordinate system (r, θ, z) and the resulting principal axes (defined by the eigenvectors). This is illustrated in eq. 21 for the angle α between the r axis and $\vec{e}_1$.

$$\alpha = \operatorname{acos}\left(\frac{\vec{r} \cdot \vec{e}_1}{\|\vec{r}\|\|\vec{e}_1\|}\right) \tag{21}$$

References

[1] MacSween, R. N. M., Burt, A. D., Portmann, B. C., Ishak, K., Scheuer, P. J., and Anthony, P. P., 1996, Pathology of the liver, Churchill Livingstone, New York.

[2] Malarkey, D. E., Johnson, K., Ryan, L., Boorman, G., and Maronpot, R. R., 2005, "New insights into functional aspects of liver morphology," Toxicologic Pathology, 33(1), pp. 27-34.

[3] Matsumoto, T., and Kawakami, M., 1982, "The unit-concept of hepatic parenchyma-a re-examination based on angioarchitectural studies," Acta Pathologica Japonica, 32(2), pp. 285-314.

[4] Matsumoto, T., Komori, R., Magara, T., Ui, T., Kawakami, M., Tokuda, T., Takasaki, S., Hayashi, H., Jo, K., Hano, H., Fujino, H., and Tanaka, H., 1979, "A study on the normal structure of the human liver, with special reference to its angioarchitecture," Jikeikai Med, 26, pp. 1-40.

[5] McCuskey, R. S., 1966, "A dynamic and static study of hepatic arterioles and hepatic sphincters," American Journal of Anatomy, 119(3), pp. 455-477.

[6] McCuskey, R. S., and Reilly, F. D., 1993, "Hepatic microvasculature - dynamic structure and its regulation," Seminars in Liver Disease, 13(1), pp. 1-12.

[7] Teutsch, H. F., 2005, "The modular microarchitecture of human liver," Hepatology, 42(2), pp. 317-325.

[8] Teutsch, H. F., Schuerfeld, D., and Groezinger, E., 1999, "Three-dimensional reconstruction of parenchymal units in the liver of the rat," Hepatology, 29(2), pp. 494-505.

[9] Marieb, E. N., and Hoehn, K., 2008, Anatomy & Physiology, Pearson Education, San Francisco.

[10] Dutkowski, P., de Rougemont, O., and Clavien, P. A., 2008, "Machine perfusion for 'Marginal' liver grafts," American Journal of Transplantation, 8(5), pp. 917-924.

[11] Fuller, B. J., and Lee, C. Y., 2007, "Hypothermic perfusion preservation: The future of organ preservation revisited?," Cryobiology, 54(2), pp. 129-145.

[12] Monbaliu, D., Debbaut, C., Hillewaert, W., Brassil, J., Laleman, W., Sainz-Barriga, M., Kravitz, D., Pirenne, J., Segers, P., 2011, "Flow competition between hepatic arterial and portal venous flow during hypothermic machine perfusion preservation of porcine livers," accepted for publication in International Journal of Artificial Organs.

[13] Jain, S., Xu, H. Z., Duncan, H., Jones, J. W., Zhang, J. X., Clemens, M. G., and Lee, C. Y., 2004, "Ex-vivo study of flow dynamics and endothelial cell structure during extended hypothermic machine perfusion preservation of livers," Cryobiology, 48(3), pp. 322-332.

[14] Monbaliu, D., and Brassil, J., 2010, "Machine perfusion of the liver: past, present and future," Current Opinion in Organ Transplantation, 15(2), pp. 160-166.

[15] Monbaliu, D., Vekemans, K., De Vos, R., Brassil, J., Heedfeld, V., Qiang, L., D'Hollander, M., Roskams, T., and Pirenne, J., 2007, "Hemodynamic, biochemical, and morphological characteristics during preservation of normal porcine livers by hypothermic machine perfusion," Transplantation Proceedings, 39(8), pp. 2652-2658.

[16] Rady, M. Y., Verheijde, J. L., and McGregor, J., 2006, "Organ donation after circulatory death: the forgotten donor?," Critical Care, 10(5).

[17] t Hart, N. A., van der Plaats, A., Leuvenink, H. G. D., van Goor, H., Wiersema-Buist, J., Verkerke, G. J., Rakhorst, G., and Ploeg, R. J., 2007, "Determination of an adequate perfusion

pressure for continuous dual vessel hypothermic machine perfusion of the rat liver," Transplant International, 20(4), pp. 343-352.

[18] Fondevila, C., Hessheimer, A. J., Taura, P., Sanchez, O., Calatayud, D., de Riva, N., Munoz, J., Fuster, J., Rimola, A., and Garcia-Valdecasas, J. C., 2010, "Portal Hyperperfusion: Mechanism of Injury and Stimulus for Regeneration in Porcine Small-for-Size Transplantation," Liver Transplantation, 16(3), pp. 364-374.

[19] Garcea, G., and Maddern, G. J., 2009, "Liver failure after major hepatic resection," Journal of Hepato-Biliary-Pancreatic Surgery, 16(2), pp. 145-155.

[20] Tanaka, K., and Ogura, Y., 2004, ""Small-for-size graft" and "small-for-size syndrome" in living donor liver transplantation," Yonsei Medical Journal, 45(6), pp. 1089-1094.

[21] Spannbauer, M. M., Oleszczuk, A., Tannapfel, A., Bluher, M., Pietsch, U. C., Hengstler, J., Donaubauer, B., Madaj-Sterba, P., Furll, M., Schuhmacher, A., Thiery, J., Hauss, J. P., and Schon, M. R., 2005, "Micro- and macrovesicular steatotic liver model for transplantation induced by ethanol and protein-deficient diet," Transplantation Proceedings, 37(1), pp. 210-211.

[22] Zhang, J. J., Meng, X. K., Dong, C., Qiao, J. L., Zhang, R. F., Yue, G. Q., and Zhong, H. Y., 2009, "Development of a New Animal Model of Liver Cirrhosis in Swine," European Surgical Research, 42(1), pp. 35-39.

[23] van der Plaats, A., 't Hart, N. A., Verkerke, G. J., Leuvenink, H. G. D., Verdonck, P., Ploeg, R. J., and Rakhorst, G., 2004, "Numerical simulation of the hepatic circulation," International Journal of Artificial Organs, 27(3), pp. 222-230.

[24] Debbaut, C., Monbaliu, D., Casteleyn, C., Cornillie, P., Van Loo, D., Masschaele, B., Pirenne, J., Simoens, P., Van Hoorebeke, L., and Segers, P., 2011, "From Vascular Corrosion Cast

to Electrical Analog Model for the Study of Human Liver Hemodynamics and Perfusion," IEEE Transactions on Biomedical Engineering, 58(1), pp. 25-35.

[25] Kennedy, A. S., Kleinstreuer, C., Basciano, C. A., and Dezarn, W. A., 2010, "Computer modeling of yttrium-90-microsphere transport in the hepatic arterial tree to improve clinical outcomes," International Journal of Radiation Oncology Biology Physics, 76(2), pp. 631-637.

[26] Mescam, M., Kretowski, M., and Bezy-Wendling, J., 2010, "Multiscale Model of Liver DCE-MRI Towards a Better Understanding of Tumor Complexity," IEEE Transactions on Medical Imaging, 29(3), pp. 699-707.

[27] Yang, Y., George, S., Martin, D. R., Tannenbaum, A. R., and Giddens, D. P., 2006, "3D modeling of patient-specific geometries of portal veins using MR images," 28th Annual International Conference of the IEEE Engineering in Medicine and Biology Society.

[28] Rani, H. P., Sheu, T. W. H., Chang, T. M., and Liang, P. C., 2006, "Numerical investigation of non-Newtonian microcirculatory blood flow in hepatic lobule," Journal of Biomechanics, 39, pp. 551-563.

[29] Ricken, T., Dahmen, U., and Dirsch, O., 2010, "A biphasic model for sinusoidal liver perfusion remodeling after outflow obstruction," Biomechanics and Modeling in Mechanobiology, 9(4), pp. 435-450.

[30] Bonfiglio, A., Leungchavaphongse, K., Repetto, R., and Siggers, J. H., 2010, "Mathematical Modeling of the Circulation in the Liver Lobule," J. Biomech. Eng., 132(11), pp. 111011(111011)-111011(111010).

[31] Wambaugh, J., and Shah, I., 2010, "Simulating Microdosimetry in a Virtual Hepatic Lobule," Plos Computational Biology, 6(4), p. e1000756.

[32] Shah, I., and Wambaugh, J., 2010, "Virtual tissues in toxicology," Journal of Toxicology and Environmental Health-Part B-Critical Reviews, 13(2-4), pp. 314-328.

[33] Greenway, C. V., and Stark, R. D., 1971, "Hepatic vascular bed," Physiol. Rev., 51(1), pp. 23-65.

[34] Maes, F., Ransbeeck, P., Van Oosterwyck, H., and Verdonck, P., 2009, "Modeling Fluid Flow Through Irregular Scaffolds for Perfusion Bioreactors," Biotechnology and Bioengineering, 103(3), pp. 621-630.

[35] Liakopoulos, A. C., 1965, "Darcy's coefficient of permeability as symmetric tensor of second rank," International Association of Scientific Hydrology, 10(3), pp. 41-48.

[36] Barbee, J. H., and Cokelet, G. R., 1971, "The Fahraeus effect," Microvascular Research, 3(1), pp. 6-16.

[37] Raghunathan, S., Evans, D., and Sparks, J. L., 2010, "Poroviscoelastic Modeling of Liver Biomechanical Response in Unconfined Compression," Annals of Biomedical Engineering, 38(5), pp. 1789-1800.

[38] Beezer, R. A., 2010, "A First Course in Linear Algebra," University of Puget Sound, Tacoma, Washington, USA.

Table captions

Table 1. Coordinates of the cubes (characteristic length 50 µm) dissected from the simulation geometry (characteristic length 0.15 mm; Fig. 2b). These cubes were used to calculate the permeability tensor. The boundaries of the cubes are given by specifying the upper and lower limits of the r, θ and z coordinates, respectively. The origin (0, 0, 0) is located at the center of the sample dissected from the dataset (see also Fig. 3).

Table 2. Results of the permeability tensor and 3D porosity calculations. For each of the fifteen cubes as defined in Table 1, the permeability tensor K as well as the porosity ε were studied. For every permeability coefficient and the porosity, the mean value, standard deviation, p-value resulting from the Shapiro-Wilk test and median were calculated. The 3D porosity is distributed around a mean value of 14.3%.

Figure captions

Figure 1. The human liver macrocirculation (left) and microcirculation (right). The liver receives blood from the hepatic artery (HA) and portal vein (PV). The HA and PV branch until they reach the level of the microcirculation at the typical hexagonal lobules (right panel). Every lobule receives blood from its periphery through the hepatic arterioles and portal venules. These are located in the portal triads at each corner of the lobule. Consequently, HA and PV blood is mixed in the sinusoids and drained radially towards the central vein. On their turn, the central veins cluster towards the outflow hepatic veins (HV) and vena cava inferior.

Figure 2. (a) Scanning electron microscopic image of the sample that was dissected out of the human liver cast. The intertwined and interconnected liver sinusoids are clearly visible in this cast sample representing three liver lobules. (b) 3D reconstruction of the simulation geometry of the case in which a pressure difference is established in the r direction. The origin (0, 0, 0) is located at the center of the sample. The inflow and outflow guidances are clearly visible, as well as an illustration of the surface mesh density. The meshes existed of approximately 1 million triangular surface elements and 9 million tetrahedral volume elements capturing the sinusoidal geometrical features.

Figure 3. Dissection of the sample used for the numerical simulations: transectional (left) and longitudinal side (right) views of a hexagonal lobule with indications of the location of the dissected sample. A cube with dimensions (0.15 x 0.15 x 0.15 mm^3) was dissected of a liver lobule. The dissected cube was oriented in such a way that its z axis was approximately parallel to the direction of the central vein (longitudinal according to the liver lobule). In addition, the r

and θ axis were approximately oriented along the radial and circumferential directions, respectively, according to the hexagonal transection of the lobule.

Figure 4. Static pressure visualization on the boundaries of the 3 computational fluid dynamics models. The flow direction is from top to bottom (along the r, θ and z axis, respectively). The top plane was set to a velocity inlet, and the bottom plane to a pressure outlet. The pressure difference for the r and θ simulations are similar within a range of approximately 0 - 170 and 0 - 180 Pa, respectively. The z simulation pressure difference is typically smaller, ranging approximately from 0 to 100 Pa.

Figure 5. Visualization of the streamlines (color coded according to the velocity scale) in combination with the translucent pressure contours. The streamlines clearly indicate the preferential pathways followed by the fluid flow. In addition, the figures clearly illustrate higher velocities at locations where the sinusoids are narrow.

Figure 6. Wall shear stress distribution color map visualized on the boundaries of the 3 computational fluid dynamics models. The flow direction is from top to bottom (along the r, θ and z axis, respectively). Wall shear stresses were typically very low in the major part of all simulation geometries. At the level of narrow channels, wall shear stress increased to higher values.

Figure 7. Histograms of the wall shear stress distribution on the walls of a cube centrally located in the simulation geometry for each of the three models (flow in the r, θ and z directions). This corresponds to cube 1 as defined in Table 1. In all cases, wall shear stress was typically in the range of 0 to 1 Pa for the major part of the geometry.

Tables

Table 1.

Cube	r_{min} [µm]	r_{max} [µm]	θ_{min} [µm]	θ_{max} [µm]	z_{min} [µm]	z_{max} [µm]
1	-25	25	-25	25	-25	25
2	-50	0	0	50	0	50
3	0	50	0	50	0	50
4	-50	0	-50	0	0	50
5	0	50	-50	0	0	50
6	-50	0	0	50	-50	0
7	0	50	0	50	-50	0
8	-50	0	-50	0	-50	0
9	0	50	-50	0	-50	0
10	-25	25	-25	25	0	50
11	-25	25	-25	25	-50	0
12	-25	25	-50	0	-25	25
13	-25	25	0	50	-25	25
14	0	50	-25	25	-25	25
15	-50	0	-25	25	-25	25

Table 2.

Cube	k_{rr} [m^2]	$k_{\theta r}$ [m^2]	k_{zr} [m^2]	$k_{r\theta}$ [m^2]	$k_{\theta\theta}$ [m^2]	$k_{z\theta}$ [m^2]	K_{rz} [m^2]	$k_{\theta z}$ [m^2]	k_{zz} [m^2]	ε
1	3.80E-14	1.11E-14	-1.31E-14	-8.27E-15	1.88E-14	4.96E-15	-2.22E-14	-5.77E-15	3.66E-14	1.58E-01
2	2.06E-14	1.47E-15	-1.21E-14	2.35E-15	2.65E-14	2.42E-14	-2.99E-15	6.77E-15	7.14E-14	1.74E-01
3	3.57E-14	-6.39E-15	1.32E-14	3.86E-15	2.48E-14	1.12E-15	1.40E-15	2.08E-15	1.03E-14	1.82E-01
4	7.93E-15	3.13E-15	-3.76E-15	7.11E-15	1.76E-14	-6.14E-15	-5.27E-15	-8.93E-15	3.68E-14	1.26E-01
5	1.94E-15	1.11E-16	-1.23E-15	1.45E-15	2.87E-15	1.03E-15	-1.68E-15	1.88E-15	3.14E-15	1.10E-01
6	1.78E-14	-5.34E-15	-7.63E-15	-8.17E-15	1.17E-14	3.05E-15	-1.63E-14	-3.11E-16	4.09E-14	1.35E-01
7	6.95E-15	1.07E-15	-7.59E-15	-1.76E-15	3.95E-15	2.73E-15	-9.78E-15	2.38E-15	1.57E-14	1.23E-01
8	5.25E-15	-7.04E-16	-1.34E-15	-9.26E-16	4.78E-15	-4.02E-16	-6.16E-16	1.61E-15	9.67E-15	1.36E-01
9	3.11E-15	-1.23E-15	-2.21E-15	-6.28E-15	3.21E-15	1.22E-15	-1.61E-15	-1.50E-15	4.30E-15	8.60E-02
10	2.51E-14	5.64E-16	7.57E-15	1.14E-15	2.38E-14	1.01E-15	-7.20E-15	-2.21E-15	3.43E-14	1.64E-01
11	1.53E-14	-3.45E-15	-1.05E-14	-6.57E-14	6.93E-14	2.50E-14	-1.89E-14	2.32E-15	4.75E-14	1.80E-01
12	1.24E-14	1.15E-14	-4.86E-15	2.02E-15	2.32E-14	-7.07E-15	-2.46E-15	-8.81E-15	1.04E-14	1.34E-01
13	3.09E-14	5.17E-15	-5.45E-15	-4.88E-15	7.52E-15	3.48E-15	-2.46E-14	-3.27E-15	4.61E-14	1.63E-01
14	1.82E-14	2.77E-15	-1.27E-14	-1.30E-15	2.62E-15	3.62E-15	-9.13E-15	-1.06E-15	1.03E-14	1.18E-01
15	3.69E-14	7.76E-15	-1.67E-14	-4.68E-15	1.78E-14	5.56E-15	-1.31E-14	-4.65E-15	4.11E-14	1.57E-01
Mean	**1.84E-14**	**1.84E-15**	**-5.22E-15**	**-5.60E-15**	**1.72E-14**	**4.23E-15**	**-8.95E-15**	**-1.30E-15**	**2.79E-14**	**1.43E-01**
Stdev	**1.25E-14**	**5.33E-15**	**7.93E-15**	**1.72E-14**	**1.69E-14**	**9.00E-15**	**8.31E-15**	**4.42E-15**	**2.02E-14**	**2.80E-02**
P-value	**2.11E-1**	**5.82E-1**	**3.16E-1**	**6.73E-6**	**1.04E-3**	**1.31E-3**	**1.67E-1**	**5.98E-1**	**8.81E-2**	**6.15E-1**
Median	**1.78E-14**	**1.07E-15**	**-5.45E-15**	**-1.29E-15**	**1.76E-14**	**2.73E-15**	**-7.20E-15**	**-1.06E-15**	**3.43E-14**	**1.36E-01**

Figures

Fig1.tiff

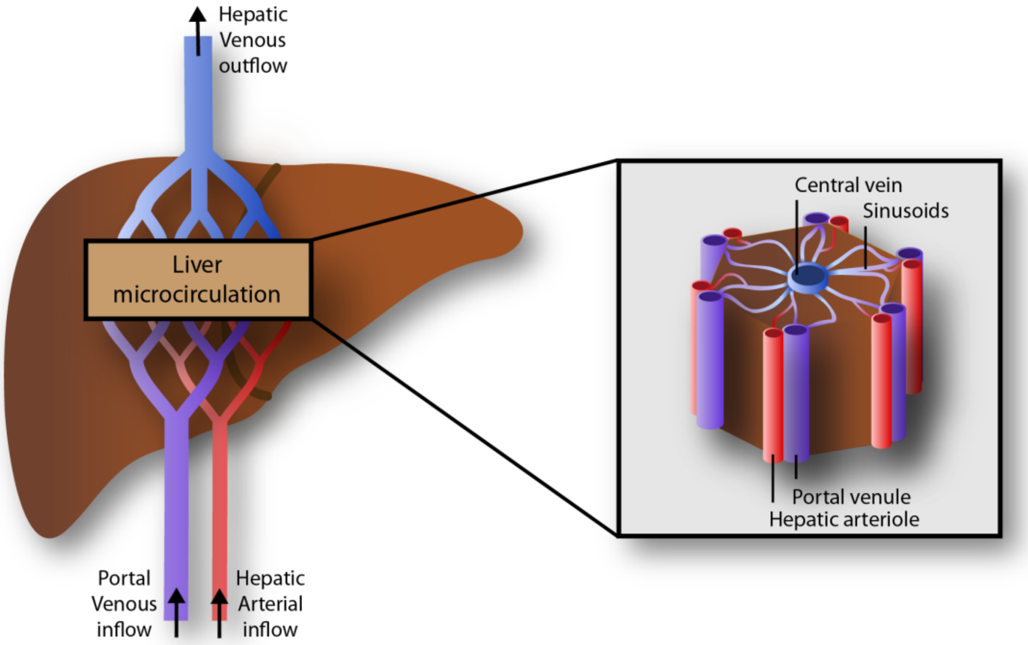

Fig2.tiff

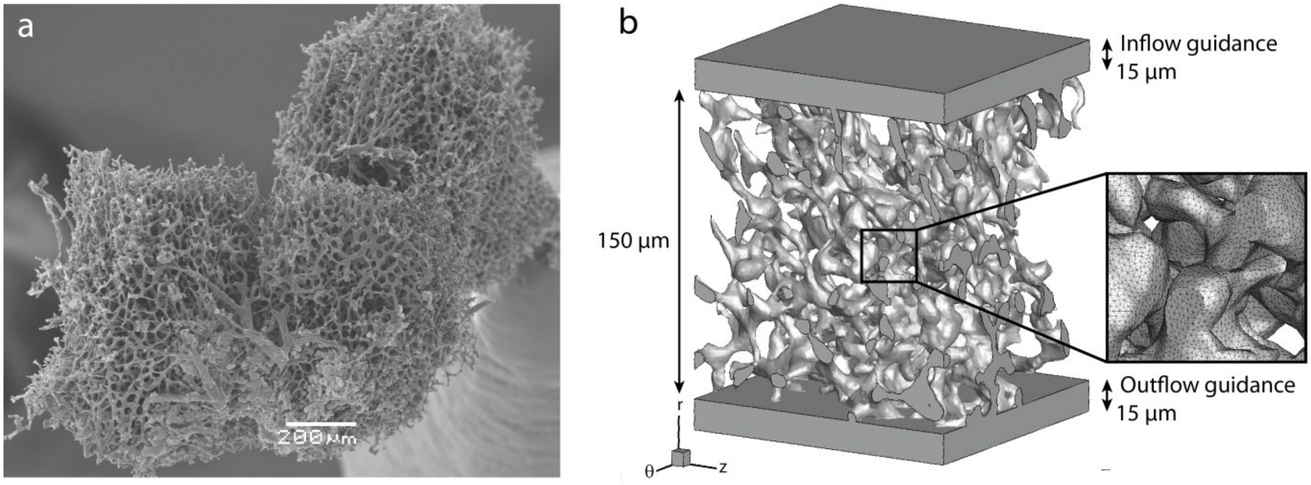
a
200 µm
b
Inflow guidance
15 µm
150 µm
Outflow guidance
15 µm
r
θ
z

Fig3.tiff

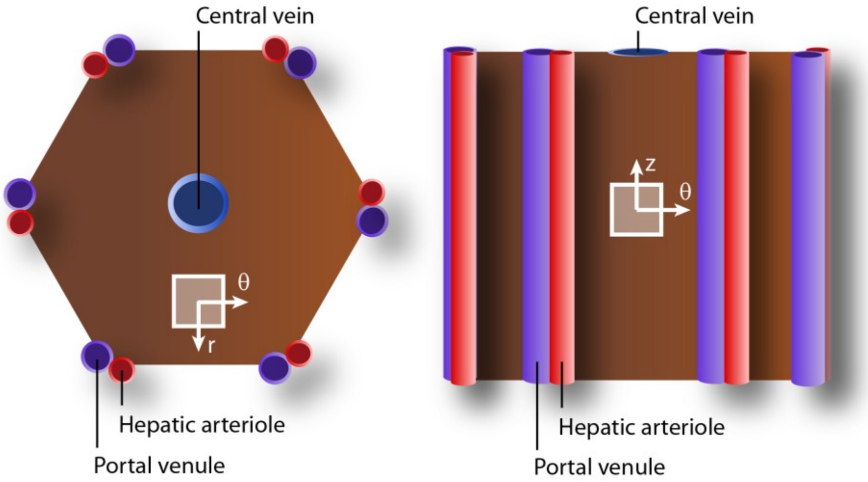
Central vein
θ
r
Hepatic arteriole
Portal venule
Central vein
z
θ
Hepatic arteriole
Portal venule

Fig4.tiff

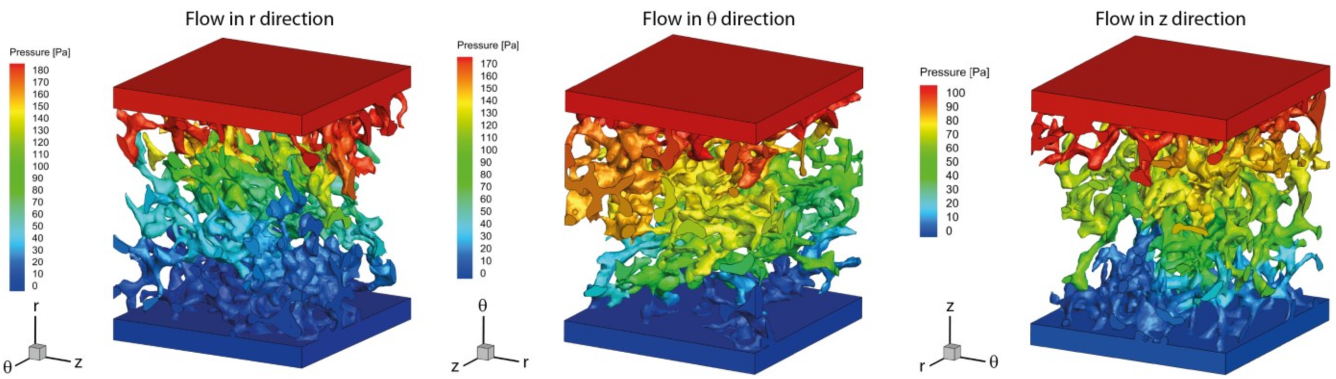
Flow in r direction

Flow in θ direction

Flow in z direction

Fig5.tiff

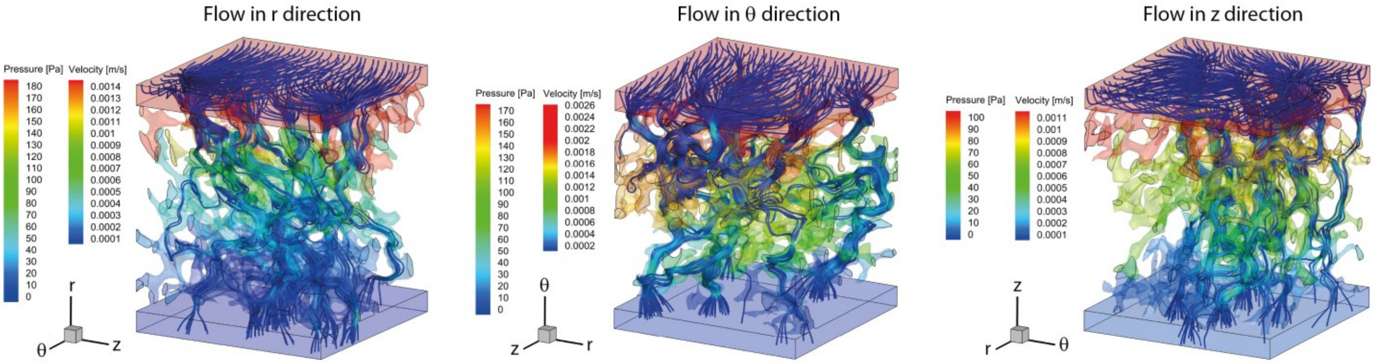

Flow in r direction

Flow in θ direction

Flow in z direction

Fig6.tiff

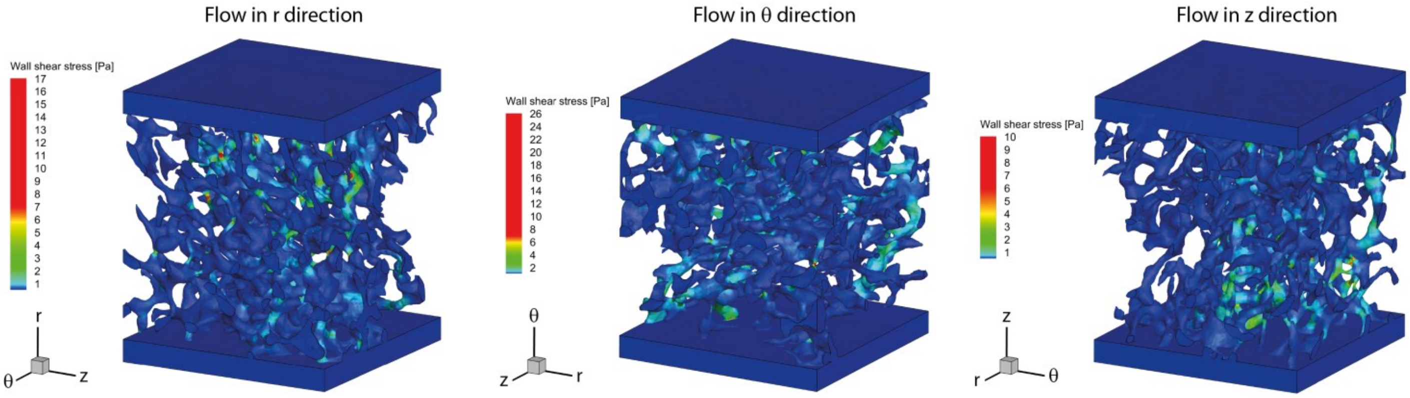
Flow in r direction
Wall shear stress [Pa]
17
16
15
14
13
12
11
10
9
8
7
6
5
4
3
2
1
r
θ
z
Flow in θ direction
Wall shear stress [Pa]
26
24
22
20
18
16
14
12
10
8
6
4
2
θ
z
r
Flow in z direction
Wall shear stress [Pa]
10
9
8
7
6
5
4
3
2
1
z
r
θ

Fig7.tiff

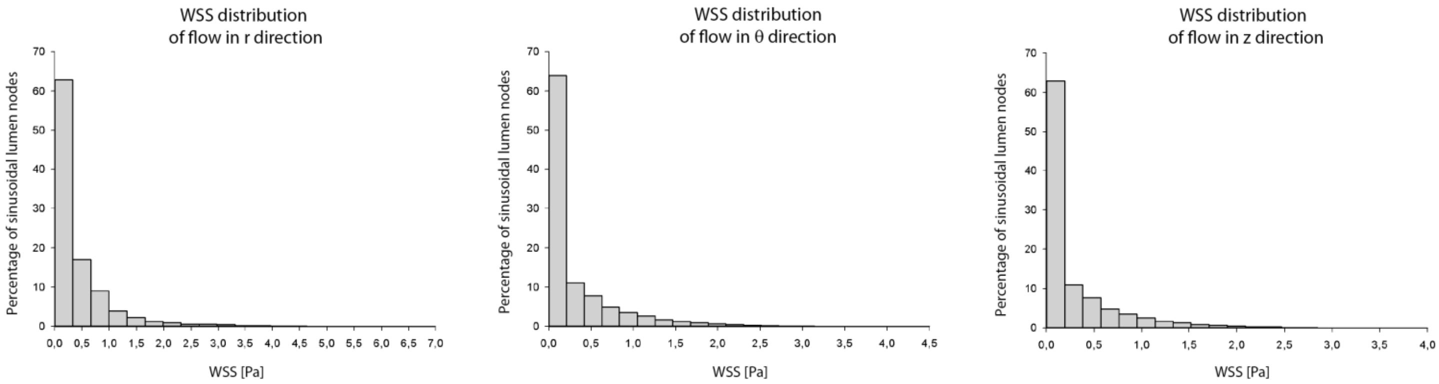
WSS distribution
of flow in r direction
Percentage of sinusoidal lumen nodes
0
10
20
30
40
50
60
70
0,0 0,5 1,0 1,5 2,0 2,5 3,0 3,5 4,0 4,5 5,0 5,5 6,0 6,5 7,0
WSS [Pa]
WSS distribution
of flow in θ direction
Percentage of sinusoidal lumen nodes
0
10
20
30
40
50
60
70
0,0 0,5 1,0 1,5 2,0 2,5 3,0 3,5 4,0 4,5
WSS [Pa]
WSS distribution
of flow in z direction
Percentage of sinusoidal lumen nodes
0
10
20
30
40
50
60
70
0,0 0,5 1,0 1,5 2,0 2,5 3,0 3,5 4,0
WSS [Pa]